Internal Wave Interferometry

Internal Wave Interferometry

Manikandan Mathur* and Thomas Peacock†

Department of Mechanical Engineering, MIT, 77 Massachusetts Avenue, Cambridge, Massachusetts 02139, USA

(Received 10 January 2010; published 15 March 2010)

Internal waves are a ubiquitous and significant means of momentum and energy transport in the oceans, atmosphere, and astrophysical bodies. Here, we show that internal wave propagation in nonuniform density stratifications, which are prevalent throughout nature, has a direct mathematical analogy with the classical optical problem of a Fabry-Perot multiple-beam light interferometer. We rigorously establish this correspondence, and furthermore provide the first experimental demonstration of an internal wave interferometer, based on the theory of resonant transmission of internal waves.

DOI: 10.1103/PhysRevLett.104.118501 PACS numbers: 92.05.Bc, 47.35.Bb, 47.55.Hd, 92.10.Hm

Internal gravity waves are propagating disturbances within the body of a stable, density-stratified fluid. They play important roles in dissipating barotropic tidal energy in the ocean [1] and transporting linear and angular momentum in the atmosphere [2] and astrophysical bodies [3], respectively; and for applications, such as deep-water drilling [4] and air travel [5], they are a significant concern. Thus, understanding internal wave propagation is both geophysically and practically important.

An intriguing aspect of internal wave propagation is the underlying dispersion relation, which requires orthogonality between phase and group velocity. A consequence of this dispersion relation is that spatially-localized forcing at a frequency ω within the body of a constant density stratification $N = \sqrt{(-g/\rho_0)(d\rho/dz)} > \omega$ produces internal wave beams that propagate at an angle $\theta = \pm\sin^{-1}(\omega/N)$ with respect to the horizontal [6]; here, g is gravity, ρ_0 is the characteristic fluid density and $d\rho/dz$ is the background density gradient. These wave beams possess a spectrum of spatial wavelengths that is determined by the size of the generation source, and have been reported in the ocean and atmosphere, where they are excited by tidal flow past sea-floor topography [7–9] and thunderstorms [10], respectively.

In geophysical settings, the background density stratification is characteristically nonuniform. For example, N attains relatively large values near the thermocline in comparison to the deep ocean [7], and layers of relatively large and small N are distributed vertically throughout the atmosphere [11]. Such vertical variation of N plays a crucial role in the propagation of internal waves following their generation. A recent study [12], for example, showed that the presence of a nonuniform stratification helps explain the apparent vanishing of an internal wave beam off the Hawaiian Islands [8]. This work built upon prior studies of plane wave propagation in nonuniform stratifications [13,14].

The aforementioned study [13] theoretically predicts the possibility of resonant transmission of internal waves through regions of sharply changing N. In this Letter, we identify that the phenomenon of resonant transmission of internal waves has a direct mathematical analogy with the classical problem of a Fabry-Perot multiple-beam light interferometer [15]. Our result builds on a previous attempt to determine internal wave equivalents of classical light phenomena, in which internal wave diffraction was experimentally studied [16], although without any established connection with the Huygen-Fresnel principle. Furthermore, we provide the first experimental evidence of an internal wave interferometer.

Theory.—In a classical multiple-beam light interferometer, a downward-propagating, plane, monochromatic light wave is incident on a pair of identical parallel surfaces that have the same properties for both upward and downward incident waves. The surfaces are separated by a distance H, and each surface transmits a fraction T of the incident light energy and reflects the remaining fraction $R = 1 - T$ [Fig. 1(a)]. The fraction of incident energy transmitted by the arrangement is [15]:

$$T_e = \left[1 + F\sin^2\left(\frac{\delta}{2}\right)\right]^{-1}, \tag{1}$$

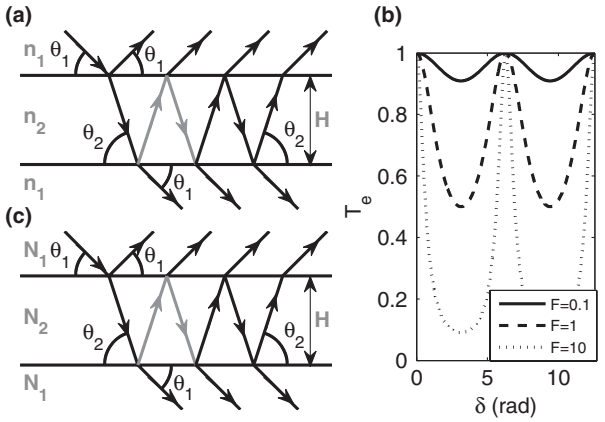

FIG. 1. (a) Ray paths in a classical multiple-beam light interferometer. n_1 and n_2 are the refractive indices of the optical media outside and between the surfaces, respectively. (b) Energy transmission coefficient T_e as a function of δ for three different values of F. (c) Internal wave ray paths for a stratification with an N_2 layer sandwiched between semi-infinite N_1-layers.

where $F = \frac{4R}{(1-R)^2}$ and $\delta = \frac{4\pi H}{\lambda} n_2 \sin\theta_2$ is the phase shift upon traversing the grey path shown in Fig. 1(a). Here, n_1 and n_2 are the refractive indices for the media outside and between the parallel surfaces, respectively, θ_1 and θ_2 are the corresponding light-ray propagation angles satisfying $n_1 \cos\theta_1 = n_2 \cos\theta_2$, and λ is the wavelength of the incident light. The value of T_e oscillates between distinct minima of $(1 + F)^{-1}$ and maxima of 1 as δ, and thus λ varies [Fig. 1(b)], giving rise to selective transmission of certain wavelengths. The maxima occur when $\delta = 2n\pi$ (where n is an integer), corresponding to constructive interference between neighboring transmitted rays. Larger values of R, and thus F, produce a greater range for T_e, with values of $T_e \approx 0$ possible for $R \approx 1$.

By analogy, for internal waves, one considers a layer of constant stratification N_2 and thickness H sandwiched between semi-infinite layers of constant stratification N_1 [Fig. 1(c)]. A downward-propagating, linear plane wave of horizontal wave number k and propagation angle $\theta_1 = \sin^{-1}(\omega/N_1)$ is incident from above on the N_2 layer, in which the angle of energy propagation is $\theta_2 = \sin^{-1}(\omega/N_2)$. Ignoring viscous and non-Boussinesq effects, continuity of velocity and pressure at the sharp interfaces between the regions of differing stratification requires the fraction of incident energy flux transmitted to the lower N_1 layer to be:

$$T_e = \left[1 + \frac{1}{4}\left(\frac{\cot\theta_1}{\cot\theta_2} - \frac{\cot\theta_2}{\cot\theta_1}\right)^2 \sin^2(kH\cot\theta_2)\right]^{-1}, \quad (2)$$

which is identical to Eq. (1) under the substitutions $F = \frac{1}{4}(\frac{\cot\theta_1}{\cot\theta_2} - \frac{\cot\theta_2}{\cot\theta_1})^2$ and $\delta = -2kH\cot\theta_2$. Physically, the $N_1 - N_2$ interfaces in Fig. 1(c) play the role of the partially reflecting surfaces in Fig. 1(a), and both F and δ also retain their physical interpretations. Specifically, $F = \frac{4R}{(1-R)^2}$, where $R = (\frac{\cot\theta_1 - \cot\theta_2}{\cot\theta_1 + \cot\theta_2})^2$ is the energy reflection coefficient for plane wave transmission across a sharp $N_1 - N_2$ interface [12], and $\delta = -2kH\cot\theta_2$ is the phase difference between two rays that arrive at the same location, with one having traveled the additional path shown in grey in Fig. 1(c). In regards to the phase difference, there is a subtle difference between the optical and internal wave arrangements, as phase changes along the direction of energy propagation of a light ray whereas phase is constant along the direction of energy propagation of an internal wave ray.

In practice, molecular and/or turbulent diffusion acts to broaden $N_1 - N_2$ interfaces in physical systems. As a consequence, wavelengths that are small compared to the thickness of the broadened interface are almost completely transmitted ($T \approx 1$) [12], reducing the effectiveness of an interferometer for short wavelengths. To counter this, one can introduce evanescent layers ($N = N_e < \omega$) of thickness H_1 between the N_1 and N_2 layers, as shown in Fig. 2(a); such a scenario is not uncommon in the atmosphere [11], for example. The modified transmission coefficient still takes the general form of Eq. (1), but with $\delta = -2kH\cot\theta_2 + 2\delta_t$, where the term $2\delta_t$ accounts for the impact of the two evanescent layers. The values of R and δ_t are computed using the methods in [12,13]. In contrast to the scenario in Fig. 1(c), F now becomes a monotonically increasing function of the vertical wave number $k_z = k\cot\theta_1$, resulting in sharper transmission peaks for larger values of k_z [Fig. 2(b)]. This concept can be further extended to continuous stratifications, in which case T_e is computed using the methods in [12,14].

Experimental configuration.—Experiments were performed in a 5.5 m-long, 0.66 m-high and 0.5 m-wide glass tank. A partition wall divided the tank into a 0.35 m-wide experimental section and a 0.15 m-wide damping section, enabling waves leaving the experimental section to be directed by parabolic end walls into the damping section, thereby eliminating reflections back into the field of view. Predetermined nonlinear stratifications of salt water were established using a double-bucket system [17] that utilized a pair of peristaltic pumps for precise control of flow rates. A calibrated conductivity and temperature probe, manufactured by Precision Measurement Engineering, Inc., mounted on a linear traverse, was used to measure the stratification.

Internal wave beams were produced using a wave generator comprising a vertical stack of 82 horizontally-oscillating plates [18,19]. The generator was configured with an active region of vertical extent $L = 2.4\lambda$, where $\lambda = 7.9$ cm was the desired dominant wavelength. Upward phase propagation of the moving plates produced a downward-propagating wave beam with a vertical wave number spectrum that was essentially a sinc function [19]. The oscillation amplitude of the active plates was 5 ± 0.05 mm, with a smooth taper to zero at either end of the active region.

Velocity field measurements were made using a LaVision particle image velocimetry (PIV) system. Glass tracer particles of diameter 10 μm that seeded the salt-stratified water were illuminated by a laser light sheet, and their motion within the plane of the sheet was tracked using

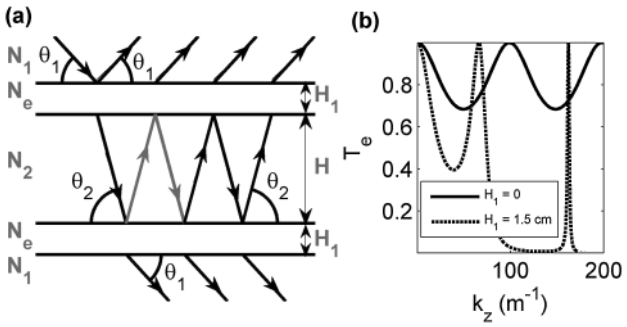

FIG. 2. (a) Ray paths in a modified stratification, with two evanescent layers added to the stratification shown in Fig. 1(c). Internal waves are evanescent in regions of stratification $N_e > \omega$. (b) Variation of T_e with k_z for an example scenario with $\theta_1 = 45°$, $N_2/N_1 = 0.8$, $N_e/N_1 = 0.4$ and $H = 0.06$ m.

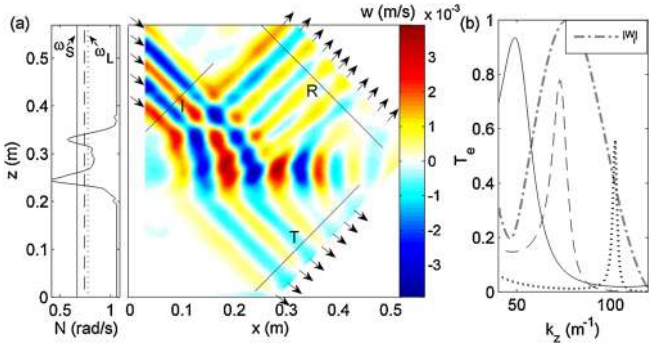

FIG. 3 (color online). (a) The stratification (left) and a snapshot of the w field (right) for an example experiment. The forcing frequency of the experiment is indicated by the dashed line superimposed on the stratification; the minimum (ω_S) and maximum (ω_L) frequencies used in this study are indicated by the solid and dotted lines, respectively. The three black lines drawn on the snapshot indicate the cross-sectional cuts used to calculate the spectra of the incident (I), transmitted (T) and reflected (R) wave beams. Arrows indicate the direction of local energy propagation. (b) T_e as a function of k_z for the stratification in (a). The three curves (solid, dashed and dotted lines) correspond to the frequencies indicated by the vertical lines in (a). $|W_I|$ (normalized by its maximum value), which is roughly constant across the ten experiments, is plotted as the dashed-dotted curve.

a 2048×2048 pixels CCD camera. Images were recorded at either 8 or 10 Hz, depending on the experiment. The planar velocity field was determined on a 128×128 spatial grid with 0.44 cm resolution. Cubic interpolation in space and Fourier filtering in time at the forcing frequency ω were used in postprocessing of the experimental data.

Results.—A snapshot of an experimental vertical velocity field w (right), and the corresponding stratification (left), are presented in Fig. 3(a). The snapshot shows the incident (I), transmitted (T) and reflected (R) wave beams at an arbitrary instant in time. The vertical dashed line superimposed on the stratification indicates the forcing frequency for the experiment ($\omega = 0.744 \pm 0.001$ rad/s), which is such that the internal waves propagate in the upper and lower regions ($N_1 = 1.05 \pm 0.01$ rad/s), and in an approximately 5 cm-thick layer ($N_2 \approx 0.82$ rad/s) lying between evanescent layers.

Figure 3(b) presents the transmission coefficient, T_e, predicted using inviscid linear theory [12,14], as a function of the vertical wave number, k_z, for three different frequencies: the minimum ($\omega_S = 0.670$ rad/s) and maximum ($\omega_L = 0.775$ rad/s) experimental frequencies, and the frequency for the experiment presented in Fig. 3(a). As ω increases, the location of the transmission peak moves to increasing values of k_z. Also shown in Fig. 3(b) is the spectrum of the vertical velocity field of the incident wave beam, $W_I(k_z)$, which was obtained for the incident cross section indicated in Fig. 3(a). Formally, $W_I(k_z) = \int_{-\infty}^{+\infty} W(\eta) \exp(-ik_z\eta/\cos\theta_1) d\eta$, where $w = \Re(We^{-i\omega t})$ and $\eta = x\sin\theta_1 + z\cos\theta_1$ is the cross beam coordinate. In practice, since the integration limits of the experimental data are restricted by the finite length of a cross section, we confirmed that W_I was not sensitive to the exact location and extent of the cross section used.

Ten experiments were performed using the stratification in Fig. 3(a), for frequencies in the range $\omega_S < \omega < \omega_L$. For each experiment, the spectra of the incident (W_I), transmitted (W_T) and reflected (W_R) wave beams were determined from the PIV data. It was found that the incident spectrum varied very little with frequency, making the task of comparing experiments more straightforward. For each experiment, the wave generator was run until the wave field reached a time periodic state, from which the experimental results were then obtained. For three of the experiments, in addition to the dominant periodic signal there were persistent weak components of the wave field that were not at the fundamental frequency, perhaps due to nonlinear effects arising from interactions between the different wave beams [20]; this was sufficiently weak, however, that it had no impact on the qualitative nature of the results.

The experimental results are presented in Fig. 4, in which $|W_I|$, $|W_T|$ and $|W_R|$ are presented as functions of k_z for the ten different experimental frequencies (and thus ten different angles of propagation of the incident wave beam). For the smallest value of ω, there is a single dominant peak in the spectra of $|W_T|$ and $|W_R|$. As ω increases, however, the location of the peak in $|W_T|$ moves to the right and, correspondingly, the spectrum of $|W_R|$ becomes double peaked, the central minimum coinciding with the peak in $|W_T|$. This evolution occurs because the

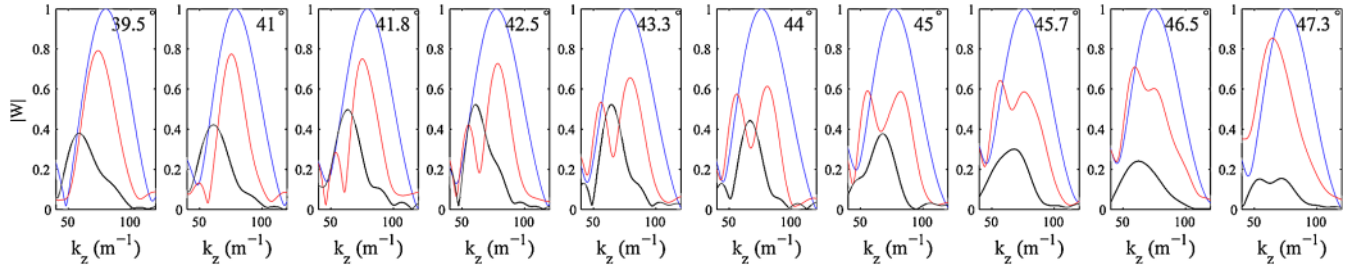

FIG. 4 (color online). Spectra of the incident (blue [dark grey]), reflected (red [light grey]) and transmitted (black) wave beams for ten experiments in which ω was increased from ω_s to ω_L. For each plot, the value of θ_1 is indicated, and $|W_I|$, $|W_R|$ & $|W_T|$ have been normalized by the corresponding maximum value of $|W_I|$.

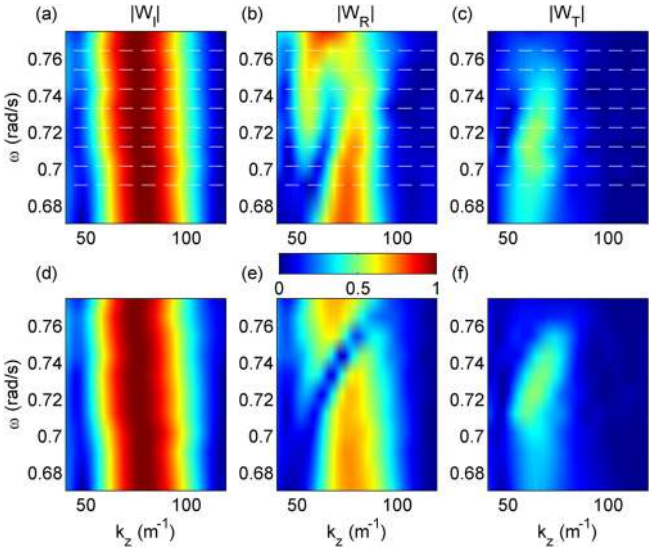

FIG. 5 (color online). (a)–(c) $|W_I|$, $|W_R|$ and $|W_T|$ (each normalized by the maximum value in $|W_I|$) as a function of k_z and ω, plotted using linear interpolation in ω of the data in Fig. 4. The white dashed lines indicate the frequencies in the ten experiments presented in Fig. 4. Note that two of the experiments were at the minimum (ω_S) and maximum (ω_L) frequencies on the vertical axis. (d)–(f) Theoretical predictions of linear viscous theory, using the experimentally measured W_I for the incident wave beam.

peak of the transmission coefficient moves to the right with increasing ω [cf. Fig. 3(b)]. As ω increases further, the spectrum of $|W_R|$ regains its single peak form, in accordance with the theoretical prediction that the peak in T_e moves to the far right-hand side of the incident spectrum, and also diminishes.

Figs. 5(a)–5(c) present a summary of the experimental results in the form of a contour plot for $40 < k_z < 120$ m^{-1} and $0.670 < \omega < 0.775$ rad/s. Corresponding theoretical predictions, which take account of viscous damping [12], are presented in Figs. 5(d)–5(f). We note that the experimental W_I was used as initial conditions for the theoretical calculations, and hence Figs. 5(a) and 5(d) are identical. This form of presentation makes it clear that the incident spectrum varied little with increasing ω. Overall, there is very good qualitative and quantitative agreement between experiment and theory. The emergence and diminution of a single peak in $|W_T|$, coinciding with the splitting and reforming of the principal peak in $|W_R|$, is evident, providing the first demonstration of the phenomenon of resonant transmission of internal waves.

Conclusions.—In conclusion, we have identified a direct mathematical analogy between an optical Fabry-Perot interferometer and the resonant transmission of internal waves in a nonuniform stratification. Furthermore, we have demonstrated this effect in a systematic set of laboratory experiments. In practice, the selective transmission of wavelengths has implications for many geophysical scenarios in the ocean and atmosphere, due to the impact of internal waves on mixing processes and the transport of energy and momentum. For laboratory experiments, this phenomenon could be exploited to generate plane waves with a very sharp spectrum.

We thank A. E. Hosoi for suggesting the form of Fig. 5. We also acknowledge help from B. Doyle and S. J. Saidi in the experiments. This work was supported by NSF Grant No. 0645529 and ONR Grant No. N00014-09-1-0282.

*manims@mit.edu
†tomp@mit.edu

[1] C. Garrett and E. kunze, Annu. Rev. Fluid Mech. **39**, 57 (2007).
[2] C. O. Hines, Can. J. Phys. **38**, 1441 (1960).
[3] C. Charbonnel and S. Talon, Science **309**, 2189 (2005).
[4] A. R. Osborne, T. L. Burch, and R. I. Scarlet, J. Pet. Technol. **30**, 1497 (1978).
[5] T. L. Clark, W. D. Hall, R. M. Kerr, D. Middleton, L. Radke, F. M. Ralph, P. J. Neiman, and D. Levinson, J. Atmos. Sci. **57**, 1105 (2000).
[6] D. E. Mowbray and B. S. H. Rarity, J. Fluid Mech. **28**, 1 (1967).
[7] F. A. Lam, L. R. M. Maas, and T. Gerkema, Deep Sea Res. I **51**, 1075 (2004).
[8] J. P. Martin, D. L. Rudnick, and R. Pinkel, J. Phys. Oceanogr. **36**, 1085 (2006).
[9] L. Gostiaux and T. Dauxois, Phys. Fluids **19**, 028102 (2007); T. Peacock, P. Echeverri, and N. J. Balmforth, J. Phys. Oceanogr. **38**, 235 (2008); H. P. Zhang, B. King, and H. L. Swinney, Phys. Rev. Lett. **100**, 244504 (2008).
[10] M. J. Alexander, J. R. Holton, and D. R. Durran, J. Atmos. Sci. **52**, 2212 (1995).
[11] R. L. Walterscheid, G. Schubert, and D. G. Brinkman, J. Geophys. Res. **106**, 31825 (2001).
[12] M. Mathur and T. Peacock, J. Fluid Mech. **639**, 133 (2009).
[13] B. R. Sutherland and K. Yewchuk, J. Fluid Mech. **511**, 125 (2004).
[14] J. T. Nault and B. R. Sutherland, Phys. Fluids **19**, 016601 (2007).
[15] S. A. Akhmanov and S. Yu. Nikitin, *Physical Optics* (Clarendon Press, Oxford, 1997).
[16] M. J. Mercier, N. B. Garnier, and T. Dauxois, Phys. Fluids **20**, 086601 (2008).
[17] G. Oster, Sci. Am. **213**, 70 (1965).
[18] L. Gostiaux, H. Didelle, S. Mercier, and T. Dauxois, Exp. Fluids **42**, 123 (2007).
[19] M. Mercier, D. Martinand, M. Mathur, L. Gostiaux, T. Peacock, and T. Dauxois, J. Fluid Mech. (unpublished).
[20] A. Tabaei, T. R. Akylas, and K. G. Lamb, J. Fluid Mech. **526**, 217 (2005); T. Peacock and A. Tabaei, Phys. Fluids **17**, 061702 (2005).